ACS Catalysis

pubs.acs.org/acscatalysis Research Article

Stabilization of Catalytic Surfaces through Core−Shell Structures: Ag−Ir/Al_2O_3 Case Study

M. Parizad,[‖] A. P. Wong,[‖] A. C. Reber, J. M. M. Tengco, S. G. Karakalos, S. N. Khanna, J. R. Regalbuto, and J. R. Monnier*

Cite This: *ACS Catal.* 2020, 10, 13352−13363 Read Online

ACCESS | Metrics & More | Article Recommendations | Supporting Information

ABSTRACT: To solve the challenges of catalyst stability and activity at high temperatures, catalyst composition and method of preparation are critical. In this context, the well-established methods of strong electrostatic adsorption and electroless deposition (ED) have been used to synthesize highly dispersed Ag/Ir on different alumina supports (δ,θ-Al_2O_3 and γ-Al_2O_3). The surface free energy (SFE) of Ag (1302 erg/cm^2) is much lower than that of Ir (3231 erg/cm^2); surface thermodynamics dictate the Ir−Ag system should arrange to give the lowest free energy of an Ag layer localized on the Ir surface to minimize the high SFE of Ir. The catalysts remained dispersed at high-temperature annealing treatments (400, 600, and 800 °C). For all Ag−Ir/δ,θ-Al_2O_3 samples, H_2 chemisorption values were higher after annealing at 400 and 600 °C than at 200 °C and were considerably higher than for the corresponding 1.0 wt % Ir/δ,θ-Al_2O_3 used as the base catalyst. X-ray diffraction data and scanning transmission electron microscopy images indicate that both monometallic catalysts sintered, but deposition of an Ag shell by ED prevented the sintering of both Ag and Ir. Temperature-programmed desorption of H_2 measurements corroborates the high H_2 uptake chemisorption experiments and indicated the additional H_2 capacity was because of more weakly bound H. Computational and X-ray photoelectron spectroscopy results suggest the excess H_2 chemisorption can be accounted for by binding up to four H atoms to single-surface Ir atoms surrounded by Ag in the shell of the bimetallic catalysts that have been pretreated at temperatures >400 °C. As a result, H_2 capacity increases from the normal adsorption stoichiometry of H/Ir = 1:1 up to as high as 4:1.

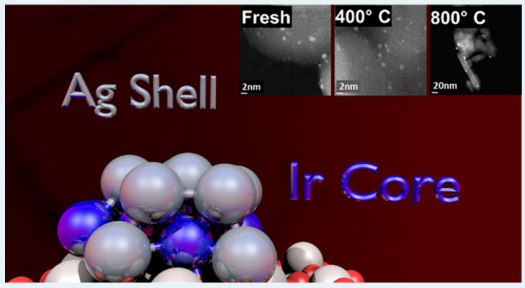

KEYWORDS: *bimetallic catalyst, H_2 chemisorption, core−shell nanoparticles, surface reconstruction, H spillover, reaction energetics, catalyst stability, electroless deposition (ED)*

1. INTRODUCTION

Catalytic stability is a focus for many industrial processes. Catalyst deactivation often limits catalyst time-on-stream through the loss of active sites by particle sintering, metal leaching, and coke formation.[1−3] Downtime of industrial processes can cause losses of millions of dollars each day; therefore, strong incentives exist to improve catalyst durability and activity. Although modifications to chemical processes can alter the rate of catalyst deactivation, in many cases harsh reaction conditions at high-temperatures such as automotive emissions, dry reforming of methane, catalytic pyrolysis, or steam reforming are unavoidable.[4−6]

Several techniques to improve catalyst stability have been developed that focus on modifications to catalyst supports to increase the interaction of metal nanoparticles with the support. Support durability can be improved by use of promoters to improve interactions with supported nanoparticles, for example, alumina doped with silica, La, Ba, or Ca.[7,8] Alternatively, incorporation of the active metal sites into the lattice of the support like those found in homogenous precipitation methods has been used.[9,10] Another method to improve nanoparticle stability is by addition of a secondary metal. Bimetallic catalysts often have increased activity, selectivity, and even stability compared to their monometallic analogs.[11−13] The inclusion of secondary metals can increase nanoparticle stability by altering the physical properties in an alloy, by changing oxidation states of one or both metals, or by selective placement of a second metal shell on the surface of another metal.[14]

Electroless deposition (ED) is a method of catalyst preparation that can test the hypothesis of improved stability by depositing a shell of a second metal on the surface of a pre-existing metal. The guidelines and methodology have been discussed in a recent book chapter.[15] Basically, ED requires a liquid phase, organic reducing agent (RA) to be activated on a

Received: July 28, 2020
Revised: October 19, 2020
Published: November 3, 2020

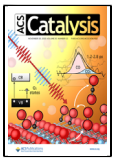

https://dx.doi.org/10.1021/acscatal.0c03297
ACS Catal. 2020, 10, 13352−13363

nanoparticle core and after activation, the reduction of a metal salt occurs to form the beginning of a shell layer. The deposition mechanism can be either catalytic or autocatalytic depending on whether the RA is adsorbed/activated on the core or the shell metal, respectively. Many different core−shell bimetallic combinations of Au−Pd, Pt−Pd, Ag−Pt, Ag−Pd, Cu−Pd, Ag−Ir, Pt−Co, Pt−Ru, Pt−Ni, and Pt−Rh, among others, have been synthesized using ED.[16−21]

In this study, we focus on enhancing the stability of catalytic surfaces by depositing an Ag layer on the surface of an Ir core supported on Al_2O_3 to form a more stable Ag layer. The Ir particles were deposited on the Al_2O_3 surface using the well-established method of strong electrostatic adsorption (SEA) developed by Regalbuto.[22,23] The surface free energy (SFE) of Ag (1302 erg/cm^2) is much lower than that of Ir (3231 erg/cm^2); the SFE of generic Al_2O_3 is stated as 805 erg/cm^2.[24,25] Thus, surface thermodynamics dictate the Al_2O_3−Ir−Ag system should arrange to give the lowest system free energy of Ir supported on Al_2O_3 with an Ag layer localized on the Ir surface to minimize the high SFE of the Ir surface. By adding a lower SFE metal shell onto a higher SFE metal core, a bimetallic system is created, which thermodynamically constrains the lower SFE metal to remain on the surface of the higher SFE metal core. Furthermore, because the support almost always has the lowest SFE, there is yet another impediment for diffusion of the shell component onto the support. Thus, it should be possible to design and synthesize numerous metal core−shell configurations to theoretically prevent sintering of the shell metal and stop the migration of the shell metal component onto the support surface. To test this hypothesis, a series of Ag coverages prepared by ED using an aqueous bath containing $Ag(CN)_2^-$ and hydrazine (N_2H_4) as RA on Ir have been synthesized and characterized following annealing at temperatures ranging from 200 to 800 °C. The stability was determined by annealing treatments followed by chemisorption, X-ray diffraction (XRD), X-ray photoelectron spectroscopy (XPS), and scanning transmission electron microscopy (STEM) measurements. Experimental results were compared to density functional theory (DFT) calculations on the same system.

2. METHODS

2.1. Computational Details. First principles theoretical studies were performed using dispersion-corrected DFT within the generalized gradient approximation proposed by Perdew, Burke, and Ernzerhof (PBE) for the exchange and correlation functional.[26] The DFT-D3 method was used to include the van der Waals corrections.[27] The computations were performed using the VASP code, and the Kohn−Sham orbitals were expanded using a plane wave basis set and the cutoff was set to 400 eV.[28,29] The support was modeled by taking a periodic cell of 72 Al atoms and 108 O atoms in the structure of α-Al_2O_3.[30] The Gibbsite model of α-Al_2O_3 included 63 Al atoms and 108 O atoms, and 27 H atoms. The model of γ-Al_2O_3 included four layers with 128 Al atoms and 196 O atoms. A dipole correction was incorporated along the z-axis of the slab. Because of the large size of the surface supercell, only the Γ point was used for Brillouin zone integration. A conjugate-gradient optimization method was used and structures were not considered optimized until the forces on the atoms were minimized to 0.01 eV/AÅ or less. For the $Ag_{11}Ir_{11}$ clusters, 25 total structures were optimized, and multiple optimizations for each structural motif were performed to make certain that the structure has found the local minimum. For the hydrogen binding studies, the hydrogen atoms were placed at 10 sites around the cluster and optimized. The lowest energy structures are reported. The geometry optimization of the cluster supported on the surface was performed with the bottom two layers of the alumina support fixed, while the top three layers were free to relax.

2.2. Experimental Details. All catalyst supports were calcined at 700 °C for 4 h before metal deposition. SEA was used to deposit the iridium anionic precursor, potassium hexachloroiridiate (K_2IrCl_6, Alfa Aesar 99.9%), on δ,θ-alumina (SASOL APA 0.2, BET surface area = 37 m^2/g) and γ-alumina (UOP VGL-25, and BET surface area = 164 m^2/g) under low pH conditions. Solutions of HCl and NaOH were used to adjust the pH to lower and higher values, respectively. Potassium silver cyanide, $KAg(CN)_2$, and potassium gold cyanide, $KAu(CN)_2$, were used as the precursors for ED, and the RAs were hydrazine and formaldehyde.

2.3. Catalyst Characterization. Metal concentrations were analyzed using a PerkinElmer 2000DV ICP−OES and a PerkinElmer AA 400. A Micromeritics 2920 Analyzer was used to determine the number of catalytically active sites by H_2 pulse chemisorption. All catalysts were first reduced at 200 °C in H_2 followed by hydrogen chemisorption at 40 °C. Annealing treatments were then performed in situ using flowing UHP argon after being passed through both deoxo and H_2O removal filters (Restek) at 200, 400, 600, and 800 °C for 4 h each followed by hydrogen chemisorption at 40 °C. All chemisorption measurements were performed immediately after pretreatment. Temperature-programmed desorption (TPD) measurements were also performed using a Micromeritics 2920 Analyzer in the continuous flow mode to determine desorption characteristics of H_2. Pretreatments in flowing Ar were also done in situ before desorption experiments were conducted. Following pretreatment, a 10% H_2/balance Ar gas flow was passed over the sample at 25 °C for 15−30 min to saturate the surface with chemisorbed H. After purging the sample for 15 min to remove residual and physically adsorbed H_2, the TPD experiment was started and the sample was heated from 20 to 420 °C at 10 °C/min. Desorbed H_2 was monitored as a positive peak in the Ar carrier stream. XRD patterns were collected using a Rigaku MiniFlex II equipped with a high sensitivity D/tex Ultra Si slit detector and a Cu Kα radiation source (λ = 1.5406 Å) operated at 30 mA and 15 kV. Scans were typically made over a 2θ range of 20−80° at a scan rate of 2.0°/min. Diffraction patterns were also obtained for the supports alone. Metal diffraction patterns were deconvoluted using Gaussian peak shapes, and the average particle sizes were estimated using the Scherrer equation with a shape factor of 0.94.

XPS analyses were carried out on a Kratos AXIS Ultra DLD XPS system with a monochromatic Al Kα source at 15 keV and 150 W at pressures below 10^{-9} torr. The X-rays were incident at an angle of 45° with respect to the surface normal. High-resolution core level spectra were measured with a pass energy of 10 eV and analysis of the data was carried out using XPSPEAK41 software. The XPS system was equipped with a hemispherical electron analyzer, a catalysis cell for in situ chemical treatments, and a load lock chamber for rapid introduction of samples without breaking vacuum. The XPS experiments were conducted using an electron gun directed on the sample for charge neutralization.

https://dx.doi.org/10.1021/acscatal.0c03297
ACS Catal. 2020, 10, 13352−13363

3. RESULTS AND DISCUSSION

3.1. Theoretical Investigations. The hypothesis was that core−shell nanoparticles will have enhanced stability when the core metal has a larger SFE than the shell metal. To test this hypothesis, we performed a series of theoretical investigations on cluster models to identify if such core−shell particles exhibit enhanced stability. The first model system was a 10 atom cluster, Ag_9X on α-alumina (0001), in which nine Ag atoms formed the shell of the core−shell cluster, and the core was a single metal atom, X; we tested X = Au, Ag, Cu, Pd, Pt, Ni, Rh, Co, Ir, Fe, and Ru, where the metals were sorted by smallest to largest calculated SFE.[31] The Ag binding energies (BEs) were calculated using eq 1, and the core metal BEs for the core element X using eq 2.

$$(\text{Ag BE}) = E(\text{Ag}_8\text{X\_Al}_2\text{O}_3) + E(\text{Ag}_{\text{atom}}) - E(\text{Ag}_9\text{X\_Al}_2\text{O}_3) \quad (1)$$

$$(\text{X BE}) = E(\text{Ag}_9\text{\_Al}_2\text{O}_3) + E(\text{X}_{\text{atom}}) - E(\text{Ag}_9\text{X\_Al}_2\text{O}_3) \quad (2)$$

The silver BEs, core metal BEs, and structures of several representative structures are shown in Figure 1A,B. The Ag BE

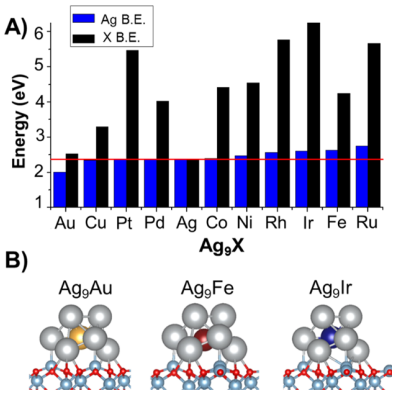

Figure 1. (A) Ag and core BE for element X of Ag_9X on α-Al_2O_3(0001). (B) Structure of Ag_9Au, Ag_9Fe, and Ag_9Ir on α-Al_2O_3(0001). Silver atoms are silver, aluminum atoms are light blue, oxygen atoms are red, and Au, Fe, and Ir are gold, red, and blue, respectively.

is a measure of the stability of the cluster, and if Ostwald ripening is the dominant mechanism for sintering,[32−34] then the Ag BE is a good proxy for the amount of sintering. The Ag BE of Ag_{10} is 2.37 eV, so we can consider the cluster to have enhanced stability if the Ag BE is greater than this value and can consider the cluster to have a reduced stability if the Ag BE is less than this value. The Ag_9 clusters with the greatest Ag BEs occur when the core metal is Ru, Fe, and Ir; Ag BEs are 2.74, 2.64, and 2.60 eV, respectively. Ru has the largest SFE, Fe has the second largest, and Ir has the third largest. Computationally, Rh, Ni, and Co also increase the Ag BE, while Pd, Pt, Cu, and Au decrease the Ag BE, although the decrease is only around 0.02 eV for the case of Au. This implies that for these clusters, sintering will be reduced in the case of Ru, Fe, and Ir, although the Ag BE compares the stability of the Ag_9X cluster to the Ag_8X cluster (after removal of one of the Ag atoms), so electronic shell effects can affect the results.[35] Ru, Fe, and Ir are all large SFE metals, which is consistent with our hypothesis that large SFE core metals will enhance stability and inhibit sintering.

The binding of the core metal X is also shown in Figure 1A and is proportional to the total BE of the bimetallic clusters. The core metal BE of the bimetallic clusters is consistently larger than for Ag. This is not necessarily a measure of the stability of the bimetallic particle versus monometallic particles because the mixing energy between the monometallic clusters and the bimetallic clusters must be compared to determine if mixing is thermodynamically favored. The greater BE of the X atom reveals that core metals such as Ir, Rh, and Ru bond most strongly to Ag than Ag to itself, so clusters with these cores should have larger total stability. Essentially, the bonding between Ag and X is greater than the bonding between Ag and Ag, although some changes in the interaction with the support may also affect the core metal BE, Ir has the largest core BE of the elements studied here. These metals with enhanced stability are all high SFE metals, which is consistent with our hypothesis, and the highest core metal BE for Ir suggests that it would be a reasonable choice for a core metal for the synthesis of core−metal particles with enhanced stability.

Larger Ag−Ir bimetallic nanoparticles were examined to further test the hypothesis that bimetallic core−shell particles will have enhanced stability when the core metal corresponds to a large SFE metal with a shell metal having a lower SFE. The energetics of different structures of $Ag_{11}Ir_{11}$ clusters on α-Al_2O_3(0001) were examined, and by far the lowest energy structure was a core−shell structure where Ag existed as a shell on an Ir core, as shown in Figure 2. The mixing energy was

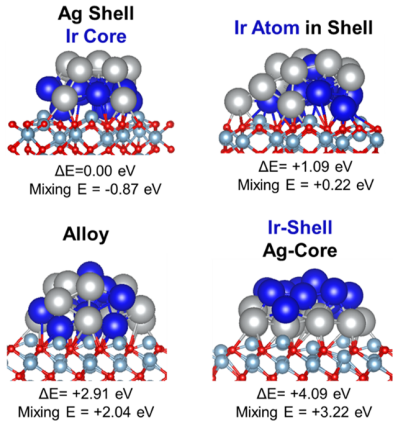

Figure 2. Structures, relative energies, and mixing energies of different $Ag_{11}Ir_{11}$ clusters on α-Al_2O_3(0001) with the Ag shell−Ir core structure (upper left), a structure with a single Ir atom in the Ag shell (upper right), a representative alloy structure (lower left), and a Ir shell−Ag core structure (lower right). Silver atoms are silver, Ir atoms are blue, aluminum atoms are light blue, and oxygen atoms are red.

calculated to be −0.87 eV using eq 3, and the negative value is evidence that the bimetallic core−shell cluster is more stable than the phase separated pure Ag and pure Ir clusters.[36]

$$E(\text{mixing}) = E(\text{Ag}_{11}\text{Ir}_{11}\text{\_Al}_2\text{O}_3) - 1/2E(\text{Ag}_{22}\text{\_Al}_2\text{O}_3) - 1/2E(\text{Ir}_{22}\text{\_Al}_2\text{O}_3) \quad (3)$$

A hybrid system was also investigated where a single atom of Ir is part of the shell that is otherwise made up of Ag and with an Ir core. We find this structure to be relatively low in energy

https://dx.doi.org/10.1021/acscatal.0c03297
ACS Catal. 2020, 10, 13352−13363

and is 1.09 eV less stable than the Ir−core, Ag−shell structure but significantly more stable than the other isomers, and the mixing energy is +0.22 eV. The energy difference of 1.09 eV corresponds to an energy of 0.05 eV/atom or about 300 °C, so it is not unreasonable for such structures to be found after heating at higher temperatures. For comparison, a series of alloy structures were calculated using the structure of the Ag_{22} cluster with positions of Ag or Ir randomly assigned. The lowest energy of these structures had a mixing energy of +2.04 eV, which is 2.89 eV less stable than the Ag shell−Ir core structure. For an Ir shell−Ag core structure, the cluster is 4.09 eV less stable than the Ag shell−Ir core structure. The stability of the Ir core, Ag shell structure is because of stronger bonding between the Ir atoms. This offers further evidence that bimetallic particles become significantly more energetically stable when they have a core−shell structure where the core metal is a large SFE metal such as Ir, and the shell is a low SFE metal such as Ag.

3.2. Catalyst Preparation. SEA was used to prepare the Ir catalysts. Adsorption density of the iridium precursors over δ,θ-Al_2O_3 and γ-Al_2O_3 is plotted against pH (Figure 3). In the

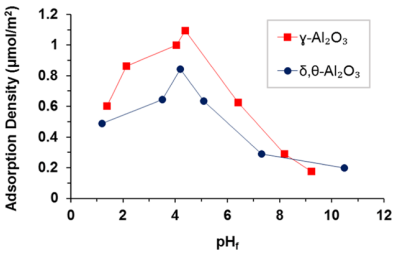

Figure 3. Adsorption of Ir complexes.

acidic pH region, anionic $IrCl_6^{2-}$ was adsorbed on the alumina supports (point of zero charge, PZC, ~ 8.4). At pH values near the PZC, only slight adsorption occurs. As the solution was acidified, the hydroxyl groups of alumina were protonated permitting the negatively charged anionic Ir complex to adsorb at greater densities. The concurrent decrease in uptake in strong acidic media can be attributed to excessively strong ionic strength, where the electrostatic charge between the protonated surface and the Ir complex was weakened from other ions in solution. The maximum adsorption densities for these alumina supports were 0.75 and 1.1 μmol/m^2 of the surface for δ,θ-Al_2O_3 and γ-Al_2O_3, respectively. This maximum adsorption occurred at a final pH ~ 4 for both aluminas.

One limitation of SEA is that the weight loading of the catalyst is limited by the maximum adsorption density of the precursor and the surface area of the support. Therefore, only a limited amount of metal was adsorbed in a single SEA cycle for the lower surface area θ,δ-Al_2O_3 support; a second cycle of SEA was required for this support. Only one SEA cycle was required for γ-Al_2O_3 because the surface area was substantially higher. The final weight loadings of Ir on δ,θ-Al_2O_3 and γ-Al_2O_3 were 1.0 and 3.2 wt % Ir, respectively. Because the surface area of γ-Al_2O_3 (164 m^2/g) was considerably higher than δ,θ-Al_2O_3 (37 m^2/g), a higher loading was used to better attain similar surface concentrations of Ir on the two supports. Initial particle sizes were below the limit of detection (<1.5 nm) using XRD line broadening. Particle sizes were thus determined by H_2 chemisorption and the data shown at a later point.

ED was used to prepare controlled, partial−shell layers on the Ir surfaces, using the methodology from previous work for bimetallic Ag−Ir core−shell structures.[20] Briefly, potassium silver cyanide, $KAg(CN)_2$, and potassium gold cyanide, KAu(CN), were used as Ag and Au precursors, and hydrazine was used as the RA. The ED bath was maintained at pH 10, above the support PZC, to prevent any electrostatic interactions between the support and either $Ag(CN)_2^-$ or $Au(CN)_2^-$. The batch kinetics of Ag deposition on δ,θ-Al_2O_3 and γ-Al_2O_3 are shown in Figure 4A,B, respectively. For ED of Ag^+, the first 30 min were used to determine whether the ED bath was thermally stable with respect to reduction of $Ag(CN)_2^-$ by the high concentration of N_2H_4. After 30 min, the 1.0% Ir/δ,θ-Al_2O_3 catalyst was added to the bath and deposition began. This was not done for deposition of $Ag(CN)_2^-$ on 3.2 wt % Ir/γ-Al_2O_3. The rates of deposition were fastest in the first 15 min when the N_2H_4 and $Ag(CN)_2^-$ concentrations were the highest. A fresh aliquot of N_2H_4 was added every 30 min to offset the instability of N_2H_4, which decomposes very quickly to evolve H_2, that is, the rate of N_2H_4 decomposition to form N_2 and H_2 is similar to the rate of activation on the Ir surface. The deposition slowed as the process continued for a number of reasons: (1) kinetics were dependent on concentrations of the Ag^+ and Au^+ salts in solution, (2) the weak affinity for autocatalytic deposition of Ag^+ on Ag^o using hydrazine as the RA, and (3) the byproduct CN^- from the reduction of the cyano salts is isoelectronic with CO, which is known to strongly adsorb on platinum group metals, which prevents further deposition.

To offset the sluggish deposition of Ag at higher coverages, the temperature of deposition was increased from 25 to 75 °C. Figure 4A shows that increasing the temperature of deposition

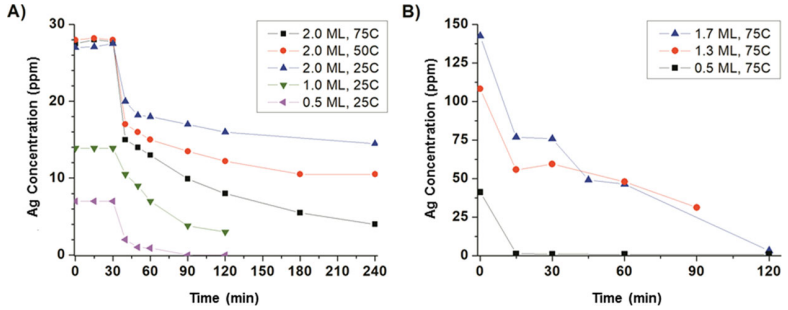

Figure 4. ED kinetics of (A) Ag on 1.0 wt % Ir/δ,θ-Al_2O_3 and (B) Ag on 3.2 wt % Ir/γ-Al_2O_3. In (A), for first 30 min, bath stability was tested; only the RA and Ag salt were present in the bath. After 30 min, 1.0 wt % Ir/δ,θ-Al_2O_3 added to the ED bath.

https://dx.doi.org/10.1021/acscatal.0c03297
ACS Catal. 2020, 10, 13352−13363

from 25 to 50 to 75 °C substantially increased the extent of deposition for the 2.0 ML target loading.

A summary of the bimetallic catalysts synthesized by ED is shown in Table 1. Weight percentages of the shell component

Table 1. Summary of Bimetallic Core−Shell Catalysts

core	support	shell metal	shell wt %	θ_{target} (ML)	θ_{theo} (ML)	θ_{exp} (ML)
1.0 wt % Ir	δ,θ-Al_2O_3	Au	0.24	0.5	0.43	0.18
		Ag	0.14	0.5	0.52	0.22
			0.21	1.0	0.81	0.40
			0.24	2.0	0.92	0.62
			0.35	2.0	1.31	0.87
			0.47	2.0	1.77	0.93
3.2 wt % Ir	γ-Al_2O_3	Ag	0.73	0.5	0.41	0.80
			1.5	1.3	0.85	0.88
			2.8	1.7	1.60	0.90

and experimental coverages were determined by atomic absorption spectroscopy and H_2 chemisorption following reduction at 200 °C, respectively. For increasing weight loadings of Ag deposited on 1 wt % Ir/δ,θ-Al_2O_3, the chemisorption results indicate Ag coverages increase from 0.22 to 0.93 ML coverage, based on monodisperse coverages of Ag on Ir (Ag/Ir = 1). Because at 25 °C and following pretreatment at 200 °C, Ag does not dissociatively adsorb H_2, the coverage of Ag on Ir can be determined from the reduction in H_2 uptake compared to the monometallic, 1 wt % Ir/δ,θ-Al_2O_3. The chemisorption analyses are discussed in more detail in Figure 9 and Table 3, where anomalous H_2 uptakes are described for annealed Ag−Ir bimetallic catalysts. From Table 1, we see that ED of 0.14 wt % Ag lowers the H_2 uptake by 22% relative to the monometallic 1 wt % Ir sample; thus, the coverage of Ag on Ir is θ_{Ag} = 0.22, and so on. However, the results for 3.2 wt % Ir/γ-Al_2O_3 showed only a marginal increase in Ag coverage (0.8 to 0.9) as the weight loading of Ag deposited by ED varies from 0.73 to 2.8 wt % Ag. It should be noted in passing that the dispersion of the Ir particles on the 3.2 wt % Ir/γ-Al_2O_3 was much higher at 1.0, so the unusually small Ir particles from the SEA preparation may have caused the unexpected behavior and changed Ag coverage from monodisperse (Ag/Ir = 1) to some other value.

Chemisorption values for the unmodified 1.0 wt % Ir and 3.2 wt % Ir samples gave H_2 uptakes corresponding to dispersions of 0.49 and 1.0, respectively, with calculated particle sizes of 2.3 and 1.1 nm, also respectively.[37] The fractional coverages of Ag on Ir are shown graphically in Figure 5. After deposition, this series of catalysts with different coverages was then annealed at increasing temperatures (400, 600, and 800 °C) to determine catalyst stability.

3.3. Particle Size Analysis. The particle sizes of these catalysts were examined using STEM images and XRD patterns. Comparisons will be made with the H_2 chemisorption results discussed in much greater detail in a later section. We note that the particle sizes of the catalysts are summarized in Table 2. The initial particle sizes of the monometallic Ir catalyst on δ,θ-Al_2O_3 were d_{chem} = 2.3 nm, d_n = 1.4 nm (number average from STEM), and d_{XRD} = <2 nm. After the annealing treatments of 200, 400, 600, and 800 °C, the final particle sizes of the monometallic 1 wt % Ir/δ,θ-Al_2O_3 were d_{chem} = 21 nm, d_n = 43 nm, and d_{XRD} = 26 nm. The two particle size measurements obtained from chemisorption and XRD are

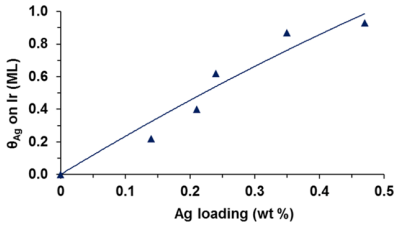

Figure 5. Coverage of Ag on Ir using chemisorption vs loading of Ag for the δ,θ-Al_2O_3 support. The decreased uptake in H_2 uptake with increasing amounts of Ag is presumed to represent Ir coverage by Ag.

Table 2. Summary of Particle Sizes of Catalysts[a]

catalyst	T (°C)	chemisorption (nm)	XRD (nm)	STEM (nm)
1% Ir/δ,θ-Al_2O_3	200	2.3	<2	1.4
	400	2.3	<1.5	
	600	24		
	800	21	26	43
0.14% Ag−1% Ir/δ,θ-Al_2O_3	200	2.9		
	400	2.4		
	600	6.4		
	800	11	20	
0.21% Ag−1% Ir/δ,θ-Al_2O_3	200	3.8		
	400	1.4		
	600	1.6		
	800	3.8	22	
0.35% Ag−1% Ir/δ,θ-Al_2O_3	200	8.7		1.5
	400	1.2		1.6
	600	3.6		
	800	5.3	22	6.7
0.47% Ag−1% Ir/δ,θ-Al_2O_3	200	16		
	400	5.0		
	600	5.7		
	800	12	22	
3.2% Ir/γ-Al_2O_3	200	1.1	<2	
	400	1.2		
	600	8.0		
	800	17	23	56
0.73% Ag−3.2% Ir/γ-Al_2O_3	200	5.6		
	400	2.7		
	600	2.2		
	800	3.2		
1.5% Ag−3.2% Ir/γ-Al_2O_3	200	9.2		
	400	4.4		
	600	2.1		
	800	3.2		
2.8% Ag−3.2% Ir/γ-Al_2O_3	200	11		
	400	7.0		
	600	2.9		
	800	3.3		1.6

[a]For bimetallic catalysts, the particle sizes are for Ir.

in good agreement with each other. The larger particle size determined from STEM measurements is likely because of an insufficient number of particles being measured, which favors larger particle size determination. Regardless, the significant

https://dx.doi.org/10.1021/acscatal.0c03297
ACS Catal. 2020, 10, 13352−13363

increase in the particle size was because of severe metal sintering after pretreatment at high temperatures. A clear suppression of nanoparticle sintering is observed for the Ag−Ir bimetallic particles. After the high-temperature pretreatments, the XRD bimetallic particle sizes for all Ag−Ir samples were between 19 and 22 nm (shown in the inset of Figure 6).

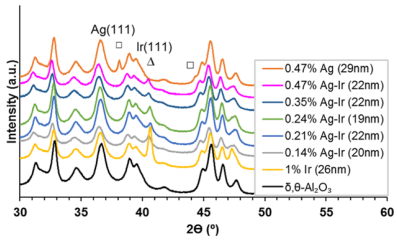

Figure 6. XRD diffraction patterns of monometallic and bimetallic catalysts supported on δ,θ-Al_2O_3 after annealing at 800 °C. XRD particle sizes are shown in the parenthesis (for bimetallic catalysts, the particle sizes are for Ir). Bimetallic catalysts contain 1 wt % Ir.

Moreover, the Ir(111) metallic peaks in the bimetallic catalysts shown at 2θ = 40.7° in Figure 6 are reduced in intensity compared to the monometallic Ir catalyst. This reduction of the Ir(111) peak suggests a bimodal distribution of Ir, where many smaller Ir particles also exist. No metallic Ag(111) peaks at 2θ = 38.1° were observed by XRD for the δ,θ-Al_2O_3 bimetallic catalysts. A monometallic Ag catalyst was annealed under the same conditions at 800 °C to compare with the bimetallic catalysts. XRD results of the annealed monometallic Ag catalyst indicated particle sintering to 29 nm. Thus, the bimetallic nanoparticles had increased resistance to sintering with regard to both the monometallic Ag and Ir counterparts. We had anticipated lower particle sizes for Ag, but the resistance of Ir to sintering was unanticipated. Because Ag and Ir do not form alloys or miscible compositions, the failure to observe Ag particles for any of the Ag−Ir bimetallic catalysts in Figure 6 also suggest Ag exists as a shell layer on the Ir core, even after annealing at 800 °C; otherwise, larger and three-dimensional Ag particles would be detected by XRD as seen for the 0.47 wt % Ag/δ,θ-Al_2O_3 sample. The existence of the Ag shell is also corroborated by the lesser extent of sintering of the Ir core component compared to monometallic 1 wt % Ir. The stabilizing effect of Ag should be greatest for a thin layer of Ag over the Ir surface.

A similar XRD analysis was performed for the γ-Al_2O_3 annealed catalysts. The initial particle size of Ir on γ-Al_2O_3 was ∼2 nm by chemisorption and <2 nm from XRD. After annealing treatments at 800 °C, Ir severely sintered as observed by a large Ir(111) peak in the XRD pattern in Figure 7. The final particle size for 3.2 wt % Ir/γ-Al_2O_3 was d_{chem} = 17 nm, d_n = 56 nm, and d_{XRD} = 23 nm. Again,

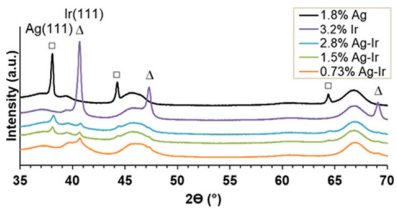

Figure 7. XRD patterns of monometallic and bimetallic γ-Al_2O_3 catalysts after annealing at 800 °C.

chemisorption and XRD bulk particle sizes are in quite good agreement with each other. When 0.73 wt % Ag was added as a shell component, both Ir and Ag were again stabilized as indicated by the absence of the Ag(111) peak and a less intense Ir(111) peak. Both Ag(111) and Ir(111) peaks existed in the higher weight loadings of Ag (1.5 and 2.8 wt %) annealed catalysts, but both peaks were less intense than either the Ag or Ir monometallic analogues. These low XRD intensities signify that a bimodal distribution of Ir and Ag nanoparticles must coexist; when XRD detected some large clusters, many small Ag−Ir clusters must have remained below the limit of XRD detection.

To summarize the XRD data, monometallic Ir and monometallic Ag catalysts were sintered on both alumina supports. Anchoring Ag as a shell by ED prevented the sintering of Ag compared with the monometallic Ag catalysts on the Al_2O_3 supports. This increased stability of Ag agrees with the SFE principles. Surprisingly, the addition of the Ag shell also decreased the sintering of Ir.

STEM was used to confirm the bimodal distribution and stabilization of the Ag−Ir nanoparticles. In Figure 8, STEM

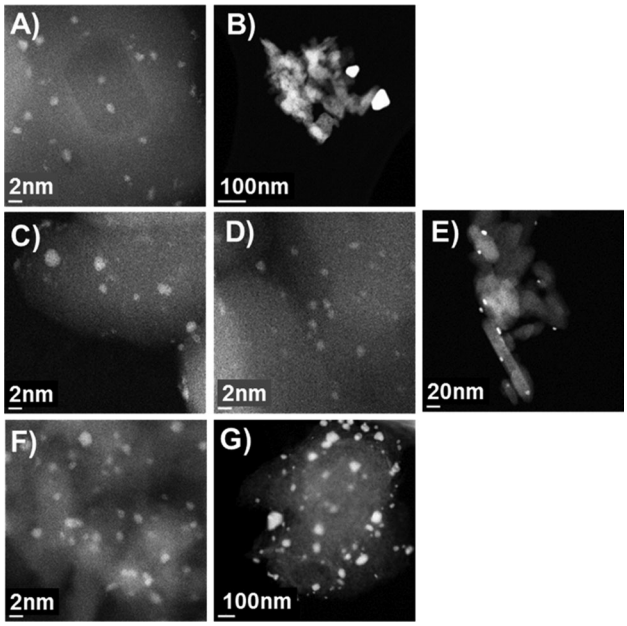

Figure 8. STEM images (with particle size distributions in Figure S1) of (A) 1% Ir/δ,θ-Al_2O_3 fresh; (B) 1% Ir/δ,θ-Al_2O_3 at 800 °C; (C−E) 0.35% Ag−Ir/δ,θ-Al_2O_3 at 200, 400, and 800 °C, respectively; (F) 2.8% Ag−Ir/γ-Al_2O_3 at 800 °C; and (G) 3.2% Ir/γ-Al_2O_3 at 800 °C.

images and particle size distributions are shown after the different pretreatment temperatures. The monometallic 1.0 wt % Ir/δ,θ-Al_2O_3 sintered from an initial d_n = 1.4 nm to a d_n = 43 nm (Figure 8A,B); all of the Ir existed as large particles. This severe sintering was prevented by addition of Ag. The bimetallic Ag−Ir catalyst (0.35Ag−1.0Ir wt %) started with an initial d_n = 1.5 nm and sintered to d_n = 1.6 nm and d_n = 6.7 nm after pretreatments of 400 and 800 °C, respectively (Figure 8C−E). Many of these Ag−Ir nanoparticles remained small (<5 nm) after 800 °C. The images taken after 400 °C annealing (Figure 8D) showed virtually no particle size difference from the initially prepared size. This validates Ir's resistance to sintering up to 400 °C, which was observed from

https://dx.doi.org/10.1021/acscatal.0c03297
ACS Catal. 2020, 10, 13352−13363

chemisorption in Figures 9 and 10. However, the unchanged particle size of the δ,θ-Al_2O_3 bimetallic catalysts between the

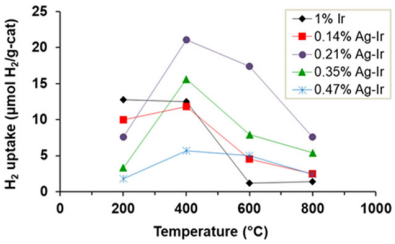

Figure 9. Chemisorption of H_2 on annealed Ag−Ir catalysts supported on δ,θ-Al_2O_3.

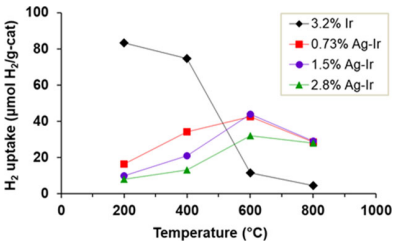

Figure 10. Chemisorption of H_2 on annealed Ag−Ir catalysts supported on γ-Al_2O_3.

initial state at 200 °C and after a pretreatment of 400 °C cannot explain the abnormally high H_2 uptake of these Ag−Ir bimetallic catalysts after pretreatments at intermediate temperatures. If an Ag shell was to sinter and expose the Ir surface, the H_2 uptake would not surpass the maximum H_2 uptake of the monometallic Ir.

A STEM comparison was also made between an annealed monometallic Ir (3.2 Ir wt %) and an annealed bimetallic Ag−Ir catalyst (2.8Ag−3.2Ir wt %) supported on γ-Al_2O_3. Both γ-Al_2O_3 catalysts were initially small, but after annealing at 800 °C, there was a large difference in the particle size (Figure 8F,G). The bimetallic Ag−Ir catalyst (Figure 8F) particle size was mostly unchanged at d_n = 1.6 nm, and the monometallic catalyst severely sintered to d_n = 56 nm (Figure 8G). The results of very little sintering for the bimetallic system over γ-Al_2O_3 agrees with the minute Ir(111) XRD peaks and high H_2 capacity after 800 °C shown in Figures 7 and 10, respectively. The STEM images of both Al_2O_3 supports at various wt loadings and Ag coverages suggest a clear indication that the bimetallic Ag−Ir catalysts are more sinter resistant. The particle size distribution for all catalysts is displayed in Figure S1.

3.4. Chemisorption Results. The chemisorption results of the δ,θ-Al_2O_3-supported Ag−Ir bimetallic catalysts are shown in Figure 9 and summarized in Table 3. The chemisorption data at 200 °C show the expected decrease in H_2 uptake as higher levels of Ag are deposited on the Ir surface. Results also show the 1.0 wt % Ir catalyst was thermally stable up to 400 °C in flowing Ar; no change in H_2 uptake from chemisorption between 200 and 400 °C was observed.

However, at temperatures ≥600 °C, the H_2 uptake decreased dramatically from 12.5 to 1.2 μmol/g catalyst, indicative of severe nanoparticle sintering. However, for all Ag−Ir samples, H_2 uptakes were actually higher after annealing at 400 and 600 °C than at 200 °C. The effect is greatest for the sample with 0.21 wt % Ag where the H_2 uptake was 3× higher

Table 3. Chemisorption Results of the Ag−Ir Bimetallic System Supported on δ,θ-Al_2O_3

	1% Ir	0.14% Ag−Ir	0.21% Ag−Ir	0.24% Ag−Ir	0.35% Ag−Ir	0.47% Ag−Ir
θ_{Ag} at 200 °C	0	0.22	0.40	0.62	0.87	0.93
conditions	H_2 uptake at 40 °C following pretreatments, (μmol H_2/g-cat)					
reduce in H_2 at 200 °C, 2 h		12.8	7.6	4.5	3.3	1.8
heat in Ar at 400 °C, 4 h	12.5	11.8	21.1	17.8	15.6	5.7
heat in Ar at 600 °C, 4 h	1.2	4.5	17.4	11.2	7.9	5.0
heat in Ar at 800 °C, 4 h	1.4	2.5	7.6	4.6	5.4	2.4

than at 200 °C. Even at 800 °C, the Ag−Ir samples exhibited higher H_2 uptakes than the unmodified Ir sample; the ordering was completely inverted from what it was at 200 °C. It is intuitive that H_2 uptake of the bimetallic catalysts should not surpass the monometallic catalyst unless the effective stoichiometry of adsorption for the H/Ir site is altered or the surface of Ag can also chemisorb H or provide adsorption sites as in the case of H-spillover or that the addition of Ag gives redispersion of Ir at high temperatures.

The same annealing/chemisorption treatments were performed on a series of Ag−Ir bimetallic catalysts supported on γ-Al_2O_3 and shown in Figure 10. 3.2 wt % Ir/γ-Al_2O_3 also exhibited similar chemisorption trends to the monometallic 1.0 wt % Ir/δ,θ-Al_2O_3 after the various annealing pretreatments. The Ir/γ-Al_2O_3 sample was also stable up to 400 °C, with only a slight deactivation compared to annealing at 200 °C. At 600 °C, there is a significant loss of active sites from 73 μmol H_2/g catalyst to 11 μmol H_2/g catalyst. The difference in the initial amounts of H_2/g adsorbed for 1.0 and 3.2 wt % loadings of Ir on Al_2O_3 catalysts was expected based simply on Ir weight loading; however, the dispersion of the Ir particles for the 1.0 wt % Ir/θ,δ-Al_2O_3 sample was 0.49 versus 1.0 for the 3.2 wt % Ir/γ-Al_2O_3 sample.

When Ag was deposited on 3.2 wt % Ir/γ−Al_2O_3, the initial H_2 uptakes at 200 °C for the bimetallic system were reduced by 80%, agreeing with higher Ag coverages giving lower initial H_2 uptakes. After annealing at 400, 600, and 800 °C, the Ag−Ir bimetallic catalysts again exhibited increased capacity for H_2 compared to the values at 200 °C indicating the same anomalous behavior. However, at no point was the H_2 capacity for the γ-Al_2O_3 bimetallic system higher than the maximum H_2 capacity of the monometallic Ir catalyst at 200 °C. This suggests the mechanism of enhancement of Ag to improve H_2 uptake may be different for ultrasmall Ir particles with dispersions ∼1. The migration of Ag into the bulk of Ir is unlikely because at a dispersion of 1.0, there is no bulk and Ag and Ir have not been reported to form alloys.[38] In this case, Ag may primarily stabilize Ir particles to prevent extreme sintering. The H_2 uptake values for the γ-Al_2O_3 bimetallic catalysts after treating at 800 °C were higher than for the monometallic Ir catalyst, which supports the ability of Ag to stabilize Ir particle sizes.

Finally, to illustrate these anomalous H_2 uptakes were not limited to Ag−Ir particles, a similar series of Au−Ir/δ,θ-Al_2O_3 catalysts were prepared that exhibited the same behavior of elevated H_2 uptake at 400 and 600 °C. A representative chemisorption plot is shown in Figure 11 that compares the

https://dx.doi.org/10.1021/acscatal.0c03297
ACS Catal. 2020, 10, 13352−13363

optimum coverages of both Ag and Au on Ir for enhanced H_2 chemisorption.

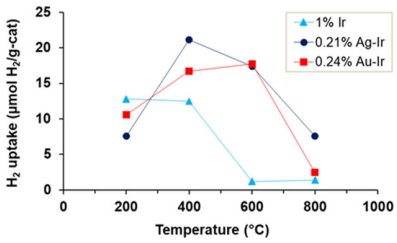

Figure 11. Comparison of Ag−Ir and Au−Ir catalysts for H_2 adsorption.

3.5. TPD of H_2. Temperature-programmed desorption of H_2 (adsorbed at 40 °C) following in situ annealing at 400 °C in flowing Ar was conducted to better understand the sites and energetics giving rise to the higher H_2 adsorption values. The TPD results in Figure 12 show the desorption spectra of unmodified 1% Ir/θ,δ-Al_2O_3 and three different coverages of Ag on Ir. All Ag−Ir catalysts show (at least) two other lower-temperature H_2 desorption peaks in addition to the H_2 desorption peak centered at ∼275 °C attributed to Ir; the larger peak was centered at 90−100 °C and the other at 170−180 °C. The peaks were observed for all bimetallic Ag−Ir samples. It was not possible to quantitatively compare desorption amounts (no response factor determined) for the different catalysts although all peak intensities were normalized to 0.10 g of the sample. Regardless, the TPD results corroborate the chemisorption experiments and indicate the additional H_2 capacity is because of more weakly bound H than normally existing on surface Ir sites. Later discussion of the XPS and DFT results indicates that H spillover onto adjacent Ag sites and/or multiple H atoms on special Ir sites are likely responsible. Most likely, H atoms adsorbed on Ag or multiple H atoms per Ir site would be more weakly adsorbed than one H per surface Ir atom.

Figure 9 shows that the Ag−Ir catalysts annealed at 800 °C exhibited higher H_2 uptakes than unmodified Ir and the results in Figure 13 confirm those results. The 1% Ir sample gave no

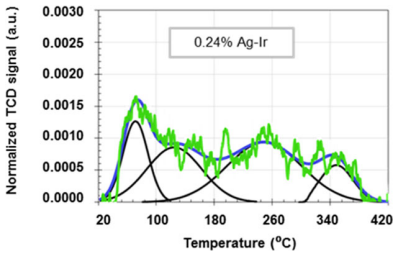

Figure 13. TPD of H_2 from 0.24% Ag−1.0% Ir/θ,δ-Al_2O_3 with θ_{Ag} = 0.62 annealed at 800 °C. There was no observable TPD of H_2 from the base 1.0% Ir/θ,δ-Al_2O_3 catalyst.

observable H_2 desorption, while the 0.24% Ag−1.0% Ir/θ,δ-Al_2O_3 sample gave measurable H_2 desorption with at least four desorption peaks, including the low-temperature peaks found after annealing at 400 °C. Thus, the unusual behavior of the Ag−Ir system persists even at 800 °C. The magnitude of the desorption peak at ∼260 °C also suggests that Ag has apparently stabilized the Ir particle from undergoing sintering.

3.6. Computational Study of H_2 Adsorption. In order to understand the observed trends in H_2 uptake on Ag/Ir nanoparticles, H_2 BEs to a model $Ag_{11}Ir_{11}$ core−shell particle were investigated. Four hypotheses were tested to determine the weakly bound H that desorbs as H_2, seen in TPD experiments. We were also interested in understanding the unusually large H_2 adsorption for the Ag−Ir particles after annealing at $T \geq 400$ °C. First, charge transfer from Ag to Ir in core−shell particles might activate the Ag surface to permit dissociative H_2 adsorption and binding directly on Ag. Second, multiple H atoms might bind to a single-surface Ir atom surrounded by Ag atoms in the shell. Third, H spillover to Ag could occur from dissociatively adsorbed H on Ir. Fourth, reconstruction could result in a core Ir atom diffusing to the surface because of energetics of H binding and the reconstruction energy might lower the BE of H on that reconstructed Ir site. To test these concepts, the BE of H atoms was determined to evaluate whether these hypotheses were energetically feasible.

The H_2 BEs on pure Ag and Ir clusters placed on α-Al_2O_3(0001) were first determined. The BE of H_2 to Ag is 0.17

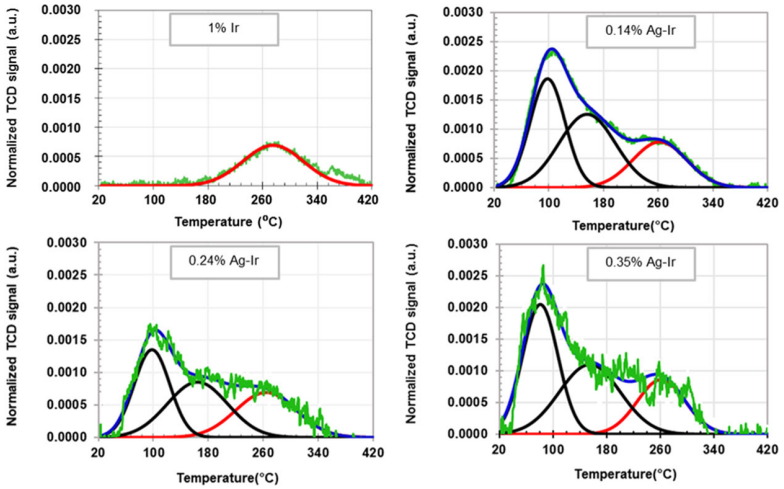

Figure 12. TPD of H_2 from 1% Ir and selected Ag−Ir bimetallic catalysts that have been annealed at 400 °C immediately before TPD experiments were conducted. Ramp rates during TPD were 10 °C/min for all samples and H_2 was initially adsorbed at 40 °C.

https://dx.doi.org/10.1021/acscatal.0c03297
ACS Catal. 2020, 10, 13352−13363

eV and the BE of H_2 to Ir is 2.99 eV, as shown in Figure 14A,B. The H_2 BE was calculated using eq 4.

$$H_2\ \mathrm{BE} = E(\mathrm{Ag}_x\mathrm{Ir}_y\_\mathrm{Al}_2\mathrm{O}_3) + E(\mathrm{H}_2) - E(\mathrm{H}_2\mathrm{Ag}_x\mathrm{Ir}_y\mathrm{Al}_2\mathrm{O}_3) \quad (4)$$

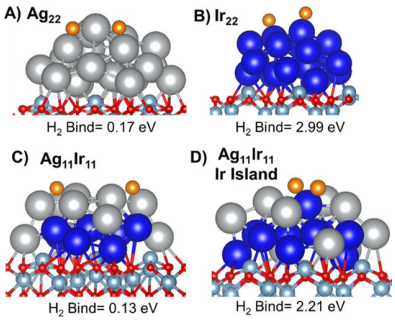

Figure 14. H_2 BE for (A) Ag_{22}, (B) Ir_{22}, (C) $Ag_{11}Ir_{11}$ core shell particles, and (D) $Ag_{11}Ir_{11}$ where one Ir atom is moved to the shell. Ag is silver, Ir is blue, and adsorbed H is orange.

The high BE of H_2 for the Ir cluster is consistent with the high desorption temperature of H_2 (~280 °C) seen in the TPD experiments, and the weak binding of Ag clusters is consistent with pure Ag particles having no H_2 uptake. The case for the Ag shell on top of Ir was next considered in Figure 14C. The BE of H_2 on Ag in the shell is 0.13 eV and is virtually the same as for pure Ag, suggesting that the Ag is not activated by Ir, so this activation was not the source of the excess and more weakly bound H_2. Figure 14D shows an Ir atom surrounded by Ag in the shell; the H_2 BE is 2.21 eV, somewhat less than what is seen for pure Ir, although still quite large. This suggests that isolated Ir atoms can strongly and dissociatively bind H_2 and that two H atoms per single Ir site are energetically favorable.

A more plausible consideration is for two H_2 molecules bound to a single Ir atom surrounded by Ag as shown in Figure 15. The first H_2 molecule dissociates and binds strongly with 2.21 eV as shown in Figure 15A, but a second H_2 molecule can also bind weakly at 0.84 eV, as indicated in Figure 15B. The H atoms are dissociatively adsorbed and are bridged between Ir and a neighboring Ag atom. The H/Ir > 1 stoichiometry agrees with the results of others for nanoparticles of Ir.[39,40] The

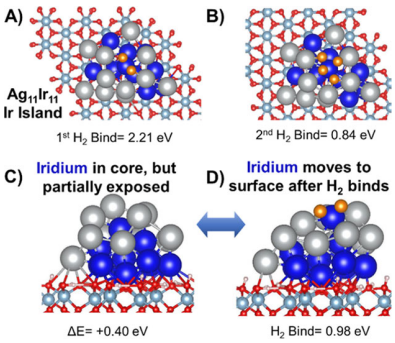

Figure 15. H_2 BE of the (A) first and (B) second H_2 molecules on $Ag_{11}Ir_{11}$ where one Ir atom is moved to the shell. (C) The structure of an isomer of $Ag_{11}Ir_{11}$ on a gibbsite alumina support. (D) The structure of $Ag_{11}Ir_{11}$ after a hydrogen molecule has bound to the partially exposed Ir atom.

calculated H_2 BE is large enough that the H/Ir stoichiometry could be as high as 4 in cases where single Ir atoms are surrounded by Ag. Because H is bridged between Ir and Ag, the BE is significantly lower than when bound to Ir alone. A third H_2 molecule appears to have a negligible BE. This very low BE suggests that H spillover is unlikely to be a source of weakly bound H. The 0.84 eV BE found for the second H_2 molecule bound to the Ir atom is a plausible energy for a source of the weakly bound H, and the large H_2 uptake. Also, this corresponds to 4 H atoms binding to a single-surface Ir atom, although this does require a structure where a single Ir atom is completely surrounded by Ag.

A final possible source of the weakly bound H is that reconstruction of the core−shell particle may weaken the BE to Ir atoms that are partially exposed. In Figure 15C, an Ir atom is "crowned" by five silver atoms in a $Ag_{11}Ir_{11}$ cluster supported on a Gibbsite alumina surface. When a H_2 molecule is brought near the Ir atom, the cluster reconstructs pulling the Ir atom out of the core. The net BE of the H_2 molecule is 0.98 eV, and this energy is lower because of the reconstruction energy of the cluster. When H_2 is removed from the exposed Ir, the Ir atom relaxes back into the core, returning to the original structure. The BE is also in the region expected for the weakly bound H_2 that desorbs in the TPD experiments.

After evaluating these different hypotheses for the weakly bound H_2 from the TPD experiments, two hypotheses have reasonable energetics. The first is that multiple H atoms bind to an Ir atom surrounded by Ag atoms. The first pair of H atoms binds quite strongly, and the second binds weakly as all four H atoms exist as bridged species between Ag and Ir. The second possibility is hydrogen-induced reconstruction of the core−shell particle, where Ir atoms that are close to the surface may bind to H_2 pulling an Ir atom out of the core, but because of the reconstruction energy, these H atoms are weakly bound. We also observed that the Ir core does not activate the Ag shell and that H spillover from Ir to Ag is energetically unfavorable. Considering that the formation of isolated Ir atoms in the Ag shell is energetically realistic, the most likely explanation is that multiple H atoms are bound to a single Ir atom in a bridged Ir−Ag configuration resulting in both weakly bound H and an unusually high uptake with a 4:1 ratio of surface H to surface Ir. The fact that ED permits these structures to be formed with a high level of certainty has permitted this correlation of experiment with theory.

3.7. XPS Results. XPS measurements were performed on the 0.24% Ag−1.0% Ir/θ,δ-Al_2O_3, and 0.24% Au−1.0% Ir/θ,δ-Al_2O_3 catalysts after in situ annealing at 400 °C in flowing Ar for 15 h in the catalysis cell attached to an ultrahigh vacuum sample chamber. The in situ treatment was conducted to permit the study of electronic interactions of the bimetallic system, which was the temperature that gave maximum H_2 chemisorption values.

Figure 16A,B shows that after annealing in Ar both Ag 3d and Ir 4f peaks shift to lower BEs by 0.5 eV and 0.8 eV, respectively, compared to their metallic states. This chemical shift is characteristic of intermetallic interactions indicating an electron transfer from Ag to Ir. Silver is an exception in photoelectron spectroscopy where there is a shift to lower BE when it transfers e^- density to electronegative elements.[41] The DFT calculations in Figure 16C,D show that the experimental chemical shifts are consistent with an Ag shell on an Ir core with the calculated Ag shift being −0.2 eV, and the Ir shift being −0.7 eV. The average charge on the Ag atoms is +0.04.

https://dx.doi.org/10.1021/acscatal.0c03297
ACS Catal. 2020, 10, 13352−13363

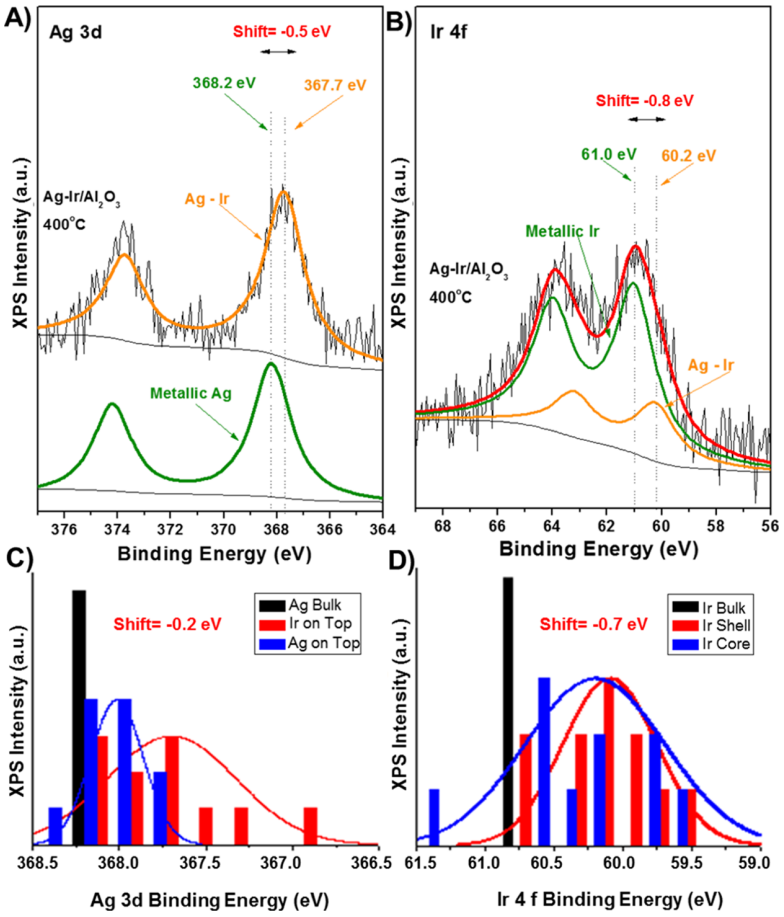

Figure 16. Electronic interaction of the 0.24% Ag−1.0% Ir/θ,δ-Al_2O_3 catalysts indicating core−shell nanoparticles after annealing at 400 °C from XPS measurements of the Ag 3d and Ir 4f core level peaks in (A,B). Panels (C,D) show DFT calculations of the chemical shifts of the corresponding XPS peaks on $Ag_{11}Ir_{11}$ on γ-Al_2O_3.

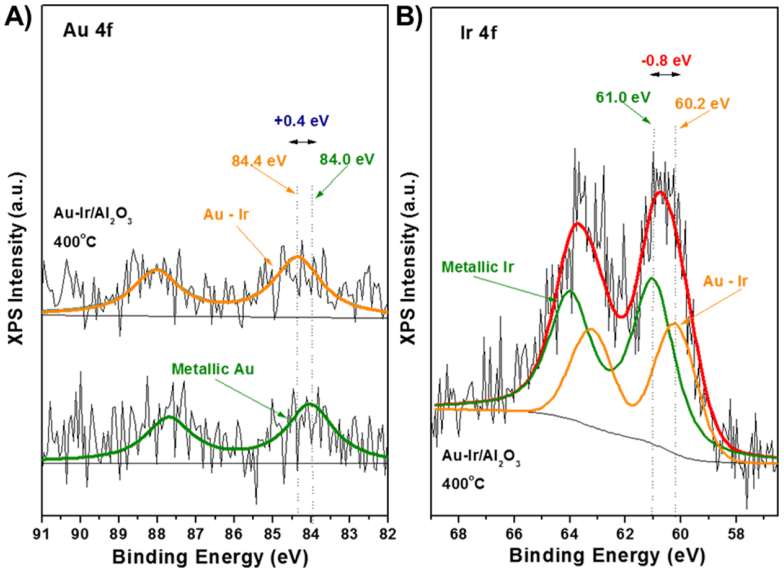

Figure 17. Electronic interaction of the 0.24% Au−1.0% Ir/θ,δ-Al_2O_3 catalysts after annealing at 400 °C as demonstrated by XPS measurements of the Au 4f and Ir 4f core level peaks.

However, when the Ag is in the core, the shift becomes −0.5 eV with the net charge on the Ag being +0.20. We have calculated these shifts on γ-Al_2O_3 because dry α-Al_2O_3 donates charge to supported metals, so α-Al_2O_3 is not an ideal model for analyzing the XPS data. For the Ir shifts, there is only a small change in the calculations for surface Ir and core Ir; core

https://dx.doi.org/10.1021/acscatal.0c03297
ACS Catal. 2020, 10, 13352−13363

Ir atoms have a shift of −0.7 eV and shell Ir atoms have a shift of −0.8 eV. While the energetic differences are small, this does not exclude the possibility that there are isolated Ir atoms surrounded by Ag in the surface layer (only one Ir atom out of a total of 11 Ir atoms) of the core−shell particle.

Both Ag and Au overlayers are expected to behave similarly[42] as we have shown in Figure 11. Han has used a combination of computational and STEM measurements to study TiO_2-supported Ir surfaces covered with a layer of Au and found that Ir atoms can diffuse through the Au layer to form "isolated" Ir atoms in a Au surface matrix, very similar to what we postulate for the Ag−Ir system.[43] In fact, similar electronic effects were observed for the XPS data in Figure 17 for the Au−Ir catalysts after annealing in Ar at 400 °C. The Au 4f peak shifts 0.4 eV to a higher BE and Ir 4f shifts 0.8 eV to a lower BE, compared to the normal metallic states of Au and Ir. These chemical shifts again indicate intermetallic interactions between the metals and an electron transfer from Au to Ir.

It has been reported that although Au alone cannot dissociate H_2, Au layers on top of Ir are reactive enough for H_2 dissociation.[44,45] The XPS results in this study provide evidence to support the chemisorption and TPD studies that H_2 chemisorption on both Ag−Ir and Au−Ir catalysts can be accounted for by strong electronic and structural differences between "as deposited" and "after annealing" bimetallic systems. The electronic interactions between Au and Ir and Ag and Ir are indicative of near-surface alloys that are able to either dissociate H_2 directly and or to provide an adsorption site for dissociatively adsorbed H.[46] The electronic transfer from Ag and Au toward Ir, together with surface segregation, can lead to enhanced catalytic activity of deposited noble metals and, possibly, Ir. Again, the key is the ability of ED to synthesize well-controlled and characterized bimetallic structures.

4. CONCLUSIONS

The combination of SEA and ED permits the formation of well-dispersed and well-controlled core−shell Ir@Ag nanoparticles on alumina supports. The Ag loading can be adjusted by changing the reaction temperature, RA, and reaction time for the ED bath. Higher Ag coverages occur at higher Ag weight loadings and coverages were determined using H_2 chemisorption following reduction at 200 °C. After high-temperature annealing in flowing Ar (400, 600, and 800 °C), H_2 chemisorption was unexpectedly high for the Ag−Ir/δ,θ-Al_2O_3 catalysts. TPD of H_2 confirmed the addition of large amounts of more weakly bound H, compared to monometallic Ir. Computational studies credit the additional H_2 capacity to changes in the adsorption stoichiometry of H/Ir (from 1:1 to 4:1) at single-atom Ir sites that are surrounded by Ag shell atoms. Consistent with the hypothesis of differential SFEs where the lower SFE component (Ag) is stabilized by deposition on the much higher SFE core metal (Ir), Ag was much more resistant to sintering. Somewhat surprising, the stability of the Ir core was also greatly enhanced. XRD, STEM, and XPS confirmed the higher stability and formation of special Ir sites. We believe this is the first instance where rational catalyst formation has been used to prepare catalysts such as these that exhibit these properties and permit an extensive suite of characterization analyses that corroborate detailed computational analyses.

■ ASSOCIATED CONTENT

Supporting Information

The Supporting Information is available free of charge at https://pubs.acs.org/doi/10.1021/acscatal.0c03297.

Particle size distribution of Ag−Ir catalysts (PDF)

■ AUTHOR INFORMATION

Corresponding Author

J. R. Monnier − *Department of Chemical Engineering, University of South Carolina, Columbia, South Carolina 29208, United States;* orcid.org/0000-0003-0809-6628; Email: monnier@cec.sc.edu

Authors

M. Parizad − *Department of Chemical Engineering, University of South Carolina, Columbia, South Carolina 29208, United States*

A. P. Wong − *Department of Chemical Engineering, University of South Carolina, Columbia, South Carolina 29208, United States*

A. C. Reber − *Department of Physics, Virginia Commonwealth University, Richmond, Virginia 23284, United States;* orcid.org/0000-0003-1013-331X

J. M. M. Tengco − *Department of Chemical Engineering, University of South Carolina, Columbia, South Carolina 29208, United States*

S. G. Karakalos − *Department of Chemical Engineering, University of South Carolina, Columbia, South Carolina 29208, United States;* orcid.org/0000-0002-3428-5433

S. N. Khanna − *Department of Physics, Virginia Commonwealth University, Richmond, Virginia 23284, United States;* orcid.org/0000-0002-9797-1289

J. R. Regalbuto − *Department of Chemical Engineering, University of South Carolina, Columbia, South Carolina 29208, United States;* orcid.org/0000-0002-5785-0749

Complete contact information is available at: https://pubs.acs.org/10.1021/acscatal.0c03297

Author Contributions

‖M.P. and A.W. contributed equally to this work

Notes

The authors declare no competing financial interest.

■ ACKNOWLEDGMENTS

The authors gratefully acknowledge the National Science Foundation for funding through the Center for Rational Catalyst Synthesis, an Industry/University Cooperative Research Center [NSF Industry/University Collaborative Research Center grant IIP1464595]. A.C.R. and S.N.K. gratefully acknowledge funding from the U.S. Air Force Office of Scientific Research, grant FA9550-18-1-0511.

■ REFERENCES

(1) Forzatti, P.; Lietti, L. Catalyst deactivation. *Catal. Today* **1999**, *52*, 165−181.

(2) Bartholomew, C. H. Mechanisms of catalyst deactivation. *Appl. Catal., A* **2001**, *212*, 17−60.

(3) Barbier, J. Deactivation of reforming catalysts by coking-a review. *Appl. Catal.* **1986**, *23*, 225−243.

(4) Srokol, Z.; Bouche, A.-G.; van Estrik, A.; Strik, R. C. J.; Maschmeyer, T.; Peters, J. A. Hydrothermal upgrading of biomass to

biofuel; studies on some monosaccharide model compounds. *Carbohydr. Res.* **2004**, *339*, 1717−1726.
(5) Shelef, M.; McCabe, R. W. Twenty-five years after introduction of automotive catalysts: what next? *Catal. Today* **2000**, *62*, 35−50.
(6) Pakhare, D.; Spivey, J. A review of dry (CO2) reforming of methane over noble metal catalysts. *Chem. Soc. Rev.* **2014**, *43*, 7813−7837.
(7) Horiuchi, T.; Chen, L.; Osaki, T.; Sugiyama, T.; Suzuki, K.; Mori, T. A novel alumina catalyst support with high thermal stability derived from silica-modified alumina aerogel. *Catal. Lett.* **1999**, *58*, 89−92.
(8) Ozawa, M. Thermal stabilization of catalytic compositions for automobile exhaust treatment through rare earth modification of alumina nanoparticle support. *J. Alloys Compd.* **2006**, *408−412*, 1090−1095.
(9) Tomiyama, S.; Takahashi, R.; Sato, S.; Sodesawa, T.; Yoshida, S. Preparation of Ni/SiO2 catalyst with high thermal stability for CO2-reforming of CH4. *Appl. Catal., A* **2003**, *241*, 349−361.
(10) Lim, S.; Wang, C.; Yang, Y.; Ciuparu, D.; Pfefferle, L.; Haller, G. L. Evidence for anchoring and partial occlusion of metallic clusters on the pore walls of MCM-41 and effect on the stability of the metallic clusters. *Catal. Today* **2007**, *123*, 122−132.
(11) Liu, X.; Wang, A.; Yang, X.; Zhang, T.; Mou, C.-Y.; Su, D.-S.; Li, J. Synthesis of Thermally Stable and Highly Active Bimetallic Au−Ag Nanoparticles on Inert Supports. *Chem. Mater.* **2009**, *21*, 410−418.
(12) Wang, D.; Villa, A.; Porta, F.; Prati, L.; Su, D. Bimetallic Gold/Palladium Catalysts: Correlation between Nanostructure and Synergistic Effects. *J. Phys. Chem. C* **2008**, *112*, 8617−8622.
(13) Oh, S.; Carpenter, J. E. Platinum-rhodium synergism in three-way automotive catalysts. *J. Catal.* **1986**, *98*, 178−190.
(14) Vogel, D.; Spiel, C.; Suchorski, Y.; Trinchero, A.; Schlögl, R.; Grönbeck, H.; Rupprechter, G. Local Catalytic Ignition during CO Oxidation on Low-Index Pt and Pd Surfaces: A Combined PEEM, MS, and DFT Study. *Angew. Chem., Int. Ed.* **2012**, *51*, 10041−10044.
(15) Diao, W.; Tengco, J. M. M.; Gaffney, A. M.; Regalbuto, J. R.; Monnier, J. R. Rational synthesis of bimetallic catalysts using electroless deposition methods. *Catalysis*; The Royal Society of Chemistry, 2020; Vol. *32*, pp 116−150.
(16) Rebelli, J.; Detwiler, M.; Ma, S.; Williams, C. T.; Monnier, J. R. Synthesis and characterization of Au-Pd/SiO2 bimetallic catalysts prepared by electroless deposition. *J. Catal.* **2010**, *270*, 224−233.
(17) Kokkinidis, G.; Papoutsis, A.; Stoychev, D.; Milchev, A. Electroless deposition of Pt on Ti-catalytic activity for the hydrogen evolution reaction. *J. Electroanal. Chem.* **2000**, *486*, 48−55.
(18) Schaal, M.; Pickerell, A.; Williams, C.; Monnier, J. Characterization and evaluation of Ag-Pt/SiO2 catalysts prepared by electroless deposition. *J. Catal.* **2008**, *254*, 131−143.
(19) Gallagher, J. R.; Li, T.; Zhao, H.; Liu, J.; Lei, Y.; Zhang, X.; Ren, Y.; Elam, J. W.; Meyer, R. J.; Winans, R. E.; Miller, J. T. In situ diffraction of highly dispersed supported platinum nanoparticles. *Catal. Sci. Technol.* **2014**, *4*, 3053−3063.
(20) Song, Y.-J.; Monnier, J. R.; Fanson, P. T.; Williams, C. T. Bimetallic Ag-Ir/Al2O3 catalysts prepared by electroless deposition: Characterization and kinetic evaluation. *J. Catal.* **2014**, *315*, 59−66.
(21) Beard, K. D.; Schaal, M. T.; Van Zee, J. W.; Monnier, J. R. Preparation of highly dispersed PEM fuel cell catalysts using electroless deposition methods. *Appl. Catal., B* **2007**, *72*, 262−271.
(22) Regalbuto, J. *Catalyst Preparation: Science and Engineering*; CRC Press, 2016; pp 297−318.
(23) Regalbuto, J. R. Electrostatic Adsorption. In *Synthesis of Solid Catalysts*; de Jong, K. P., Ed.; Wiley, 2009; pp 33−58.
(24) Overbury, S. H.; Bertrand, P. A.; Somorjai, G. A. Surface composition of binary systems. Prediction of surface phase diagrams of solid solutions. *Chem. Rev.* **1975**, *75*, 547−560.
(25) Vitos, L.; Ruban, A. V.; Skriver, H. L.; Kollár, J. The surface energy of metals. *Surf. Sci.* **1998**, *411*, 186−202.
(26) Perdew, J. P.; Burke, K.; Ernzerhof, M. Generalized Gradient Approximation Made Simple. *Phys. Rev. Lett.* **1996**, *77*, 3865−3868.
(27) Grimme, S.; Ehrlich, S.; Goerigk, L. Effect of the damping function in dispersion corrected density functional theory. *J. Comput. Chem.* **2011**, *32*, 1456−1465.
(28) Kresse, G.; Furthmüller, J. Efficient iterative schemes forab initiototal-energy calculations using a plane-wave basis set. *Phys. Rev. B: Condens. Matter Mater. Phys.* **1996**, *54*, 11169−11186.
(29) Kresse, G.; Joubert, D. From ultrasoft pseudopotentials to the projector augmented-wave method. *Phys. Rev. B: Condens. Matter Mater. Phys.* **1999**, *59*, 1758−1775.
(30) Reber, A. C.; Khanna, S. N. Effect of Embedding Platinum Clusters in Alumina on Sintering, Coking, and Activity. *J. Phys. Chem. C* **2017**, *121*, 21527−21534.
(31) Tran, R.; Xu, Z.; Radhakrishnan, B.; Winston, D.; Sun, W.; Persson, K. A.; Ong, S. P. Surface energies of elemental crystals. *Sci. Data* **2016**, *3*, 160080.
(32) Harris, P. The sintering of platinum particles in an alumina-supported catalyst: Further transmission electron microscopy studies. *J. Catal.* **1986**, *97*, 527−542.
(33) Voorhees, P. W. The theory of Ostwald ripening. *J. Stat. Phys.* **1985**, *38*, 231−252.
(34) Wettergren, K.; Schweinberger, F. F.; Deiana, D.; Ridge, C. J.; Crampton, A. S.; Rötzer, M. D.; Hansen, T. W.; Zhdanov, V. P.; Heiz, U.; Langhammer, C. High Sintering Resistance of Size-Selected Platinum Cluster Catalysts by Suppressed Ostwald Ripening. *Nano Lett.* **2014**, *14*, 5803−5809.
(35) Gamboa, G. U.; Reber, A. C.; Khanna, S. N. Electronic subshell splitting controls the atomic structure of charged and neutral silver clusters. *New J. Chem.* **2013**, *37*, 3928−3935.
(36) Ferrando, R.; Jellinek, J.; Johnston, R. L. Nanoalloys: From Theory to Applications of Alloy Clusters and Nanoparticles. *Chem. Rev.* **2008**, *108*, 845−910.
(37) Gérard Bergeret, P. G. Particle Size and Dispersion Measurements. In *Handbook of Heterogeneous Catalysis*; Ertl, G., Knozinger, H., Schüth, F., Weitkamp, J., Eds.; VCH Verlagsgesellschaft mbH, 2008.
(38) Hansen, M.; Elliott, R. P.; Shunk, F. A.; Research, I. *Constitution of Binary Alloys*; McGraw-Hill: New York, 1958.
(39) Krishnamurthy, S.; Landolt, G. R.; Schoennagel, H. J. The stoichiometry of hydrogen and CO chemisorption on Ir/$gamma;-Al2O3. *J. Catal.* **1982**, *78*, 319−326.
(40) Duivenvoorden, F. B. M.; Kip, B. J.; Koningsberger, D. C.; Prins, R. Determination of the Metal Particle Size of Supported pt, rh, and ir Catalysts. A Calibration of Hydrogen Chemisorption by Exafs. *J. Phys., Colloq.* **1986**, *47*, C8-227−C8-230.
(41) Kaspar, T. C.; Droubay, T.; Chambers, S. A.; Bagus, P. S. Spectroscopic Evidence for Ag(III) in Highly Oxidized Silver Films by X-ray Photoelectron Spectroscopy. *J. Phys. Chem. C* **2010**, *114*, 21562−21571.
(42) Ruban, A. V.; Skriver, H. L.; Nørskov, J. K. Surface segregation energies in transition-metal alloys. *Phys. Rev. B: Condens. Matter Mater. Phys.* **1999**, *59*, 15990−16000.
(43) Han, C. W.; Majumdar, P.; Marinero, E. E.; Aguilar-Tapia, A.; Zanella, R.; Greeley, J.; Ortalan, V. Highly Stable Bimetallic AuIr/TiO2 Catalyst: Physical Origins of the Intrinsic High Stability against Sintering. *Nano Lett.* **2015**, *15*, 8141−8147.
(44) Okada, M.; Nakamura, M.; Moritani, K.; Kasai, T. Dissociative adsorption of hydrogen on thin Au films grown on Ir{111}. *Surf. Sci.* **2003**, *523*, 218−230.
(45) Okada, M.; Ogura, S.; Diño, W. A.; Wilde, M.; Fukutani, K.; Kasai, T. Reactive gold thin films grown on iridium. *Appl. Surf. Sci.* **2005**, *246*, 68−71.
(46) Ferrin, P. A.; Kandoi, S.; Zhang, J.; Adzic, R.; Mavrikakis, M. Molecular and Atomic Hydrogen Interactions with Au−Ir Near-Surface Alloys. *J. Phys. Chem. C* **2009**, *113*, 1411−1417.

https://dx.doi.org/10.1021/acscatal.0c03297
ACS Catal. 2020, 10, 13352−13363